

RESEARCH ARTICLE

10.1002/2014JA020896

Key Points:

- Evidence of gravity wave dissipating into the background
- Evidence for the transition of wave into smaller scales
- Convective instability is found to be the probable cause for this event

Correspondence to:

A. Taori,
alok.taori@gmail.com

Citation:

Sivakandan, M., A. Taori, S. Sathishkumar, and A. Jayaraman (2015), Multi-instrument investigation of a mesospheric gravity wave event absorbed into background, *J. Geophys. Res. Space Physics*, 120, doi:10.1002/2014JA020896.

Received 1 DEC 2014

Accepted 22 MAR 2015

Accepted article online 25 MAR 2015

Multi-instrument investigation of a mesospheric gravity wave event absorbed into background

M. Sivakandan¹, A. Taori¹, S. Sathishkumar², and A. Jayaraman¹¹National Atmospheric Research Laboratory, Gadanki, India, ²EGRL, Indian Institute of Geomagnetism, Tirunelveli, India

Abstract We investigate a gravity wave event exhibiting dissipation noted in the mesospheric O(¹S) airglow emission image measurements, over Gadanki (13.5°N, 79.2°E), on 16 March 2012 (during 16:20–16:45 UT). These gravity waves were found to propagate from south-west to north-east directions at ~65° azimuth in OH as well as in O(¹S) images. These waves had horizontal wavelength ~21.5 km with apparent horizontal phase speed ~49 m s⁻¹ and period ~7.3 min. These waves were noted to fizzle out in turbulent patches within 15 min. To identify the causative mechanism of this event, we analyze the background wind and temperature data using the medium-frequency radar wind from Tirunelveli (8.7°N, 77.8°E), ground-based Rayleigh lidar temperature data with improved capability over Gadanki, and spaceborne Sounding of the Atmosphere using Broadband Emission Radiometry/Thermosphere Ionosphere Mesosphere Energetics and Dynamics temperature data (20:30 UT) for a latitude-longitude grid of 3–23°N, 60–100°E. Our analysis reveals that convective instability was responsible for the observed event.

1. Introduction

Since their discovery [Hines, 1960], investigation of gravity waves in various atmospheric parameters has remained a major interest to the community owing to their dominant role in the middle and the upper atmospheric variability [e.g., Fritts and Alexander, 2003]. Most of the gravity waves are generated in the lower atmosphere and propagate upward with increasing amplitudes [e.g., Fritts and Alexander, 2003]. Some of these waves attain very large amplitudes at mesospheric altitudes and get saturated and become unstable, ultimately dissipating their energy and momentum in the ambient [Fritts, 1989]. Mostly influenced by these processes, the upper mesosphere is characterized as a region of high degree of variability in short as well as long time scales [Mayr et al., 2000; Smith, 2012; Kamalakar et al., 2013].

When it comes to the measurements of short-scale gravity waves (horizontal wavelengths <50 km), the mesospheric airglow imaging and photometry are the only method which provide reliable and direct estimates [e.g., Alexander et al., 2010]. Ground-based airglow photometries are widely used to study waves having periods from 20 min to 6 h [Taori et al., 2005; Ghodpage et al., 2014], while the wide-angle imaging is a well-accepted method which provides horizontal wavelengths, propagation direction, and relative amplitudes of short-period (5–20 min) gravity waves [Taylor, 1997, and references cited therein] having their horizontal wavelengths less than 150 km. In this regard, there are several reports around the world which use airglow imaging methods detecting the horizontal wavelengths in 10 km–100 km ranges and their direction of propagation. For example, Pautet et al. [2005] investigated the gravity wave propagation from northern Australia: Wyndham (15.5°S, 128.1°E) and Katherine (14.5°S, 132.3°E) over a 10 day period in November 2001, and found horizontal wavelength of gravity waves to vary from 15 km to 45 km and that they were propagating in opposite direction from the location of lower atmospheric convective regions. Smith et al. [2006] reported strong gravity wave activity from Argentina (31.8°S, 69.3°W) which exhibited amplitudes ranging from 22% to 60% and horizontal wavelengths varying from ~10 km to 40 km. Another report by Suzuki et al. [2009] based on the image data from Kototabang (100.3°E, 0.2°S), Indonesia, during the years 2002–2005, found the horizontal wavelengths of gravity waves to vary from 10 km to 120 km with amplitudes varying from 5% to 50%. From an Indian low-latitude station Tirunelveli (8.7°N, 77.8°E) Lakshmi Narayanan et al. [2010] reported average horizontal wavelength of the observed gravity waves to be 42.9 ± 4.3 km.

As stated earlier, linear and nonlinear instabilities lead these mesospheric gravity waves to break and create turbulence before the deposition of their energy and momentum in the background medium [e.g., Fritts, 1989; Fritts and Alexander, 2003]. In this regard, although several investigators have reported the presence

of short-period, small-scale waves using airglow imaging, the evidences of breaking of waves into turbulence are very much limited. As far as we know, there are only two reports, one by *Yamada et al.* [2001], which provides clear evidence of short-period gravity wave resulting in turbulence from 34.9°N, 136.1°E, Japan, and another by *Cai et al.* [2014] from 41.7°N, 111.8°W, U.S.. The present investigation provides evidence of gravity wave absorbed into the background first time from a low-latitude Indian station.

2. Measurement Techniques

In present study we use (a) airglow image measurements to study the gravity wave features at upper mesospheric O(¹S) emission, (b) airglow photometer and (c) Rayleigh lidar for ground-based mesospheric temperature measurements from Gadanki (13.5°N, 79.2°E), (d) medium-frequency radar measurements of background winds in 80–100 km region from Tirunelveli (8.7°N, 77.8°E), and (e) mesospheric temperature measurements by spaceborne methods. Brief details of these instruments are as follows.

The National Atmospheric Research Laboratory (NARL) Airglow Imager (NAI) located at Gadanki is equipped with 24 mm of Mamiya fish eye lens. It monitors OH (peak wavelength 840 nm), O(¹S) (peak wavelength 558 nm), and O(¹D) (peak wavelength 630 nm) emissions and has a 1024 × 1024 pixels CCD as the detector. The present field of view of NAI is 90°, which avoids nonlinearity arising at higher zenith angles. As the imager is optimized for best viewing at these three wavelengths, the best images of mesospheric waves are noted in the O(¹S) emissions which originate at ~92–102 km (with a peak emission altitude of ~97 km). The exposure time used to measure the O(¹S) emissions intensities was 110 s. After capturing, the image has been analyzed and corrected for the background brightness and actual coordinates. More details of the NAI are discussed by *Taori et al.* [2013]. Further, we have corrected the images for Barrel distortion arising due to the lens curvature effect using MATLAB subroutine. This, together with the fact that only 90° full field of view is used in the present study, makes us confident that the edges shown in the images exhibit the real dimensions instead of distortions.

The mesosphere lower thermosphere photometer (MLTP) is a multi-wavelength airglow photometer with F/2 optics and full field of view 4°. It measures mesospheric OH (at 840 and 846 nm rotational lines) and O₂ (at 866 and 868 nm rotational lines) emissions together with upper mesospheric O(¹S) and thermospheric O(¹D) emission intensities with the help of seven temperature-controlled interference filters of full width at half maximum (FWHM) 0.45 nm. The temperatures are derived at OH emissions using the ratio method and O₂ emissions using the slope methods described by *Meriwether* [1984]. The MLTP uses the Hamamatsu H7421-50 photon-counting module as detector. The filter movement is synchronized with the counting unit C8855 of the photomultiplier tube for the operations. More details of photometer are described by *Taori et al.* [2011].

The Rayleigh lidar uses a neodymium: yttrium/aluminum/garnet laser with 600 mJ energy at 532 nm with a pulse repetition frequency of 50 Hz and pulse width of 7 ns. It receives backscattering with a 75 cm diameter Newtonian telescope. The received signals are isolated through an interference filter (FWHM 1.07 nm with center wavelength 532 nm) and are focused on to the photocathode of a photomultiplier tube (Hamamatsu-R3234). Temperature retrieval follows the method as described by *Hauchecorne and Chanin* [1980]. More details of the lidar system and techniques are described elsewhere [*Siva Kumar et al.*, 2003]. Generally, the model temperatures at top altitude (~100 km) are fed into the temperature retrieval algorithm due to which the reliable temperature estimates are obtained in 30–75 km altitudes. However, using the actual near-simultaneous O₂ temperature data at the top altitudes, *Kamalakar et al.* [2013] have shown that the Rayleigh lidar can be used to derive the reliable temperature estimates from 30 km to 95 km altitudes. In the present work, we have used this improvised method of temperature retrieval.

The mesospheric winds are obtained from the medium-frequency (MF) radar which operates at 2 MHz with a peak transmitter power of 25 kW from Tirunelveli. The radar makes use of spaced antenna technique and samples the horizontal winds in the 80 to 100 km altitude region using the full correlation analysis. Further details of MF radar are given elsewhere [*Rajaram and Gurubaran*, 1998].

The Sounding of the Atmosphere using Broadband Emission Radiometry (SABER) instrument on board the Thermosphere Ionosphere Mesosphere Energetics and Dynamics satellite measures limb radiance emitted from the terrestrial atmosphere in 10 selected spectral bands ranging from 1.27 to 16 μm. The

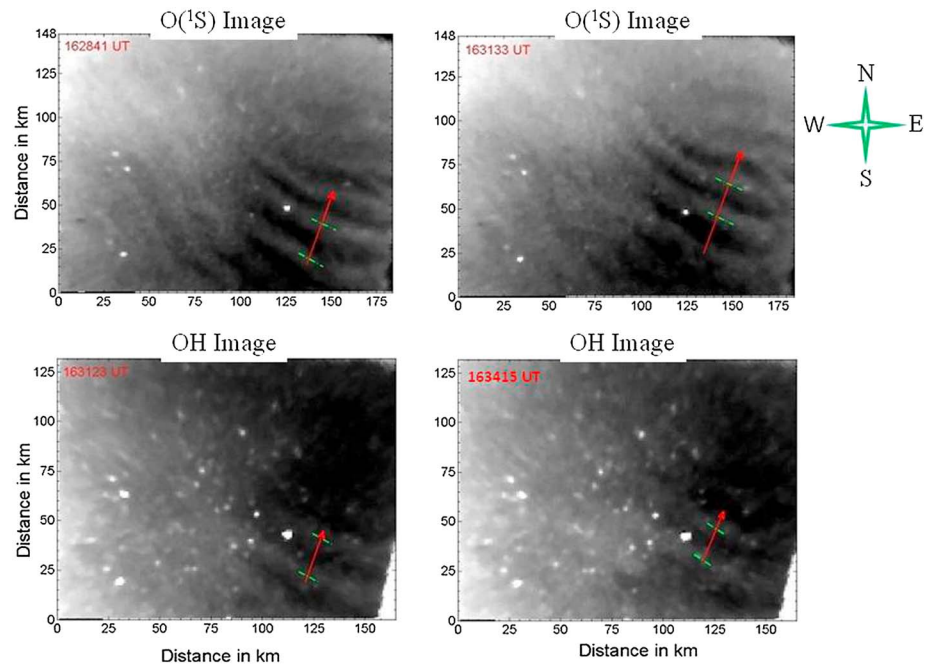


Figure 1. Sample image measurements of gravity wave in the (top) $O(^1S)$ emissions and (bottom) mesospheric OH. The right side of each image is east, while the top side depicts the north. The time of measurements is shown at the bottom of each image, while the spatial coverage of images is shown in kilometer at their peak emission altitudes. The center of image corresponds to the location of measurement, Gadanki ($13.5^{\circ}N$, $79.2^{\circ}E$).

temperature values are retrieved from SABER measurements of the atmospheric $15\ \mu\text{m}$ CO_2 limb emission. We use SABER 1.07 data which have good temperature accuracy with error in the order of $\pm 1.4\ \text{K}$ in lower stratosphere, $\pm 1\ \text{K}$ in middle stratosphere, and $\pm 2\ \text{K}$ in upper stratosphere and lower mesosphere over equatorial latitudes [e.g., Remsberg *et al.*, 2008].

The image measurements over Gadanki ($13.5^{\circ}N$, $79.2^{\circ}E$) started from 14 March 2012 and continue the operation during moonless clear-sky nights. The present investigation uses the data collected on 16 March 2012 when clear short-scale wave features were noticed. The amplitudes of these features reduced within 15 min, and small-scale patches with a possible indication of turbulence were noted. The wave signatures were noted in both OH and $O(^1S)$ data, indicating that the genesis of these waves had their origin down below and lower than $O(^1S)$ emission altitudes (sample data is shown in Figure 1). To study the temperature variations in mesospheric altitude and calculate the natural oscillation frequency/period, we utilize the improved Rayleigh lidar temperature data from Gadanki and SABER measurements for $3^{\circ}N$ – $23^{\circ}N$ and $60^{\circ}E$ – $100^{\circ}E$ grid. In the absence of collocated background wind data, we use the MF radar winds obtained from Tirunelveli ($8.7^{\circ}N$, $77.8^{\circ}E$). Although there is a difference of 4.8° latitudes, as the imager covers $\sim 2^{\circ}$ latitudes, we believe that to investigate the effects of mesospheric winds on the noted waves, it is logical to use these data instead of the model estimates.

3. Observations

3.1. Airglow Observations

Figure 1 (top) shows the sample $O(^1S)$ images exhibiting the presence of gravity waves at 97 km peak emission altitude where couple of wavefronts are indicated as straight green lines. The orientation of the image plane is shown in top-right corner of the figure with east/north being the right/top side of the images. The bright white spots show the presence of stars in the data and indicate the cloud-free viewing conditions. Time of the image measurements are shown at top left corner of each image in UT (universal time/Greenwich mean time). The spatial scale covered by the imager is shown at the left and bottom sides

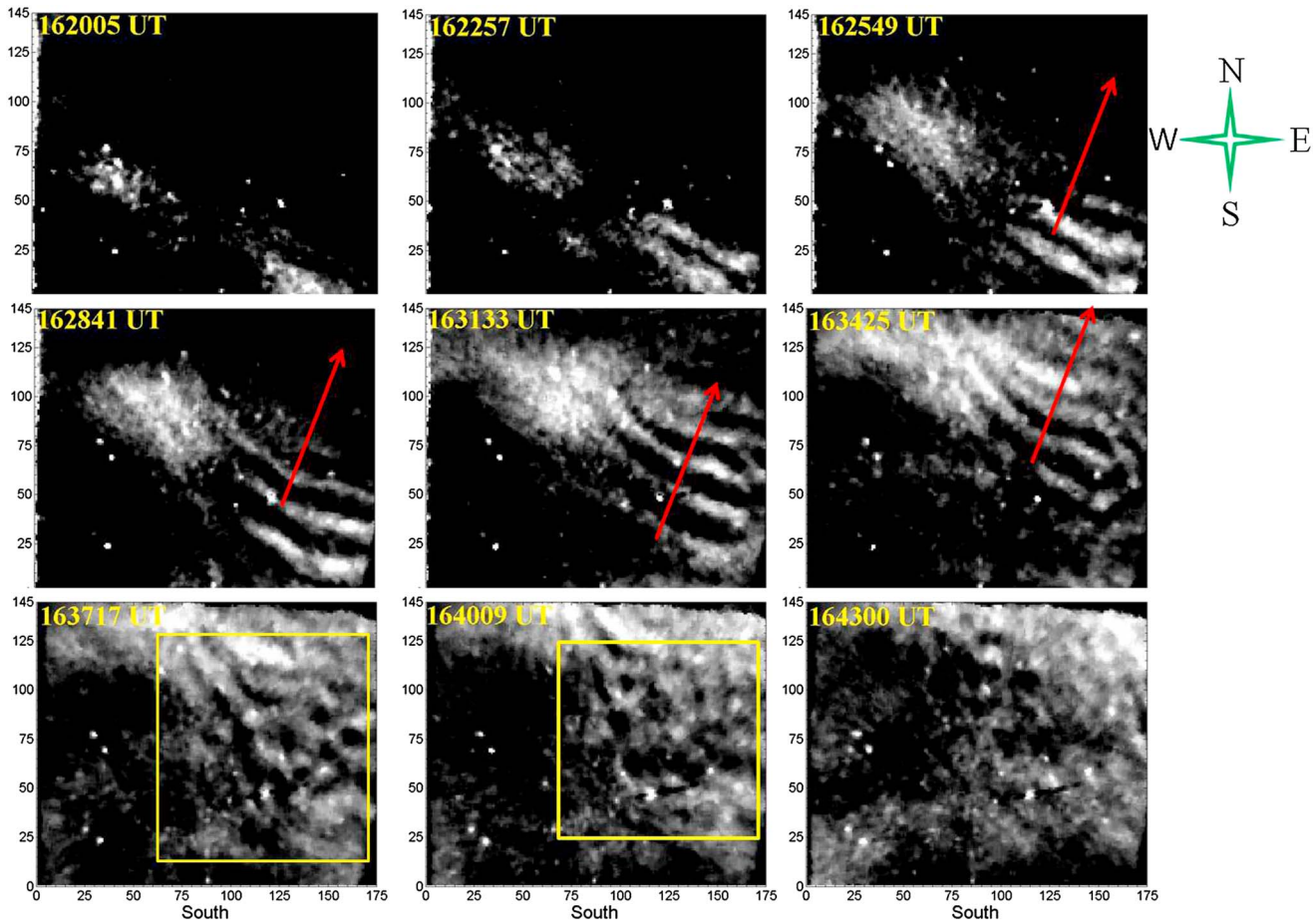


Figure 2. Sequence of $O(^1S)$ images displaying the gravity wave event from the start to finish. The time of measurement is shown as red fonts at top-left corner of each image. Note that within 20 min, the wavefronts turned into the turbulence-dominated region.

of the images. Thus, the top left image corresponds to the $O(^1S)$ emission at 16:28:41 UT, which covers approximately 180 km distance in zonal (east-west) and 148 km in meridional (north-south) direction with center of image being the location of measurements. The bottom images show the near simultaneous data corresponding to the OH emissions.

Note that the wavelength of imager observation varies from 558 nm to 840 nm and we have optimized the best focus at the detector plane around 600 nm (i.e., in between the 558 nm and 630 nm emissions). Due to this, very faint events such as shown in this case get blurred in OH data. For this reason, in present investigation, we have focused on the observed event of wave dissipation in $O(^1S)$ images. As the larger-scale wave features and slow-varying background may bias the observed intensity values and thus to further analysis of this event, we have removed hourly averaged image from each image. In doing this, we are left with only short-scale wave features during the event of the present interest. Note that the identification of phase fronts is based on the gradient method where maxima of intensity are identified. Further, the propagation velocity of waves is determined using the cross-correlation analysis between successive images. Figure 2 plots the sequence of images corresponding to $O(^1S)$ 558 nm night airglow emissions to summarize the gravity wave event of present interest. The first image corresponds to 16:20:05 UT, where gravity waves with significant amplitudes are not noted. Subsequent images show that some waves start appearing in the south-east corner of the image. The fourth image corresponding to 16:28:41 UT starts showing clear signature of gravity wave coming from the southern locations. In all these images, the red color arrow indicates the propagation direction of the wavefronts. Strikingly, the image corresponding to 16:34:25 UT starts showing the presence of gravity waves in the north-east corner and occurrence of smaller-scale features behind them in southern side. Smaller-scale features became very

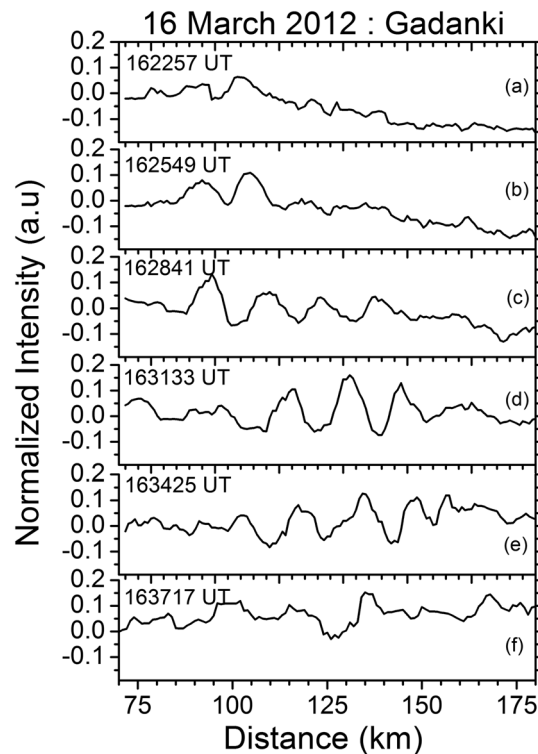


Figure 3. Intensity variation along the direction of wave propagation (from south toward north at 65° azimuth) showing the variation of amplitudes (i.e., the energy) of waves from one image to other (for the images shown in Figure 2). The time of image measurements is also shown in Figure 3.

the present case, 20 images). This removes most of the intensity biases arising due to the contribution of large-scale features as mentioned earlier in this section. Further, as far as the amplitudes of wave is concerned, it is the percentage variation from the mean values which should be important. The starting of the distance in x axis is in the south along the axis of wave propagation. As clearly noted in Figure 2, intensity variations corresponding to second image do not show a significant variation (Figure 3a). The wavelike oscillations became evident from third image (Figure 3b) and continued until fifth image (Figure 3e). It is notable that wave amplitudes increased until 16:34:25 UT (Figure 3e), while at 16:37:17 UT, the wavelike features diminished. Of importance to note is that wave train was clear only up to Figure 3d, where only southward train (75 km–100 km) shows the start of the irregular structures on the top of the feature. This irregular structure started dominating over the wave trains in further images with a total dominance over the wave trains at Figure 3f, which corresponds to 16:37:17 UT.

3.2. Mesospheric Winds

To investigate the effects of background winds, the MF radar winds were hourly averaged around the observed wave event. Figure 4a shows the altitudinal variation of zonal wind, while Figure 4b represents the meridional wind variations. It is evident that meridional winds were northward with peaks at 88–96 km altitude regions and zonal winds were westward with peaks at ~ 94 km altitudes. The winds in the direction of wave propagation are shown in Figure 4c. Note that the apparent phase velocity of waves is ~ 49 m/s, while the zonal and meridional wind estimates are -15 m/s (westward) and 12 m/s (northward), respectively, at 95–97 km altitudes. It is evident from the data that waves traveling to the west encountered filtering while the eastward propagation was possible. Also, the phase velocity of observed wave was larger than the effective winds in the direction of wave, suggesting that eastward propagation was possible. This also suggests that if source was located in south direction (which is the most often case in Indian sector [Mukherjee *et al.*, 2010]), there was no effective wind blocking for waves propagating in the north-east direction. One may argue that gradients in the horizontal winds may influence the

clear in further images which are highlighted by the yellow color box. Interestingly, the image at 16:37:17 UT shows concentric blob occurrence at the north-east portion of the image. Later images clearly show the occurrence of turbulence with no gravity wave features. We note that the horizontal scale of the gravity waves is $21.5 \text{ km} \pm 1.5 \text{ km}$ while the average phase speed of wave is $49 \text{ m/s} \pm 8.5 \text{ m/s}$. This suggests the wave period to be $7.3 \text{ min} \pm 0.3 \text{ min}$. Further, the wave was propagating at $65^\circ \pm 4.5^\circ$ azimuth angle, i.e., to the north-east direction. Please note that the error bars show standard deviation obtained from the set of images shown during the event.

To see the gravity wave amplitude (i.e., the energy) variation during the event, Figure 3 plots the intensity variation in the direction of wave propagation for the images shown in Figure 2. Note that in order to estimate the intensity variations, we have removed the background by subtracting the individual image from the hourly averaged image (in

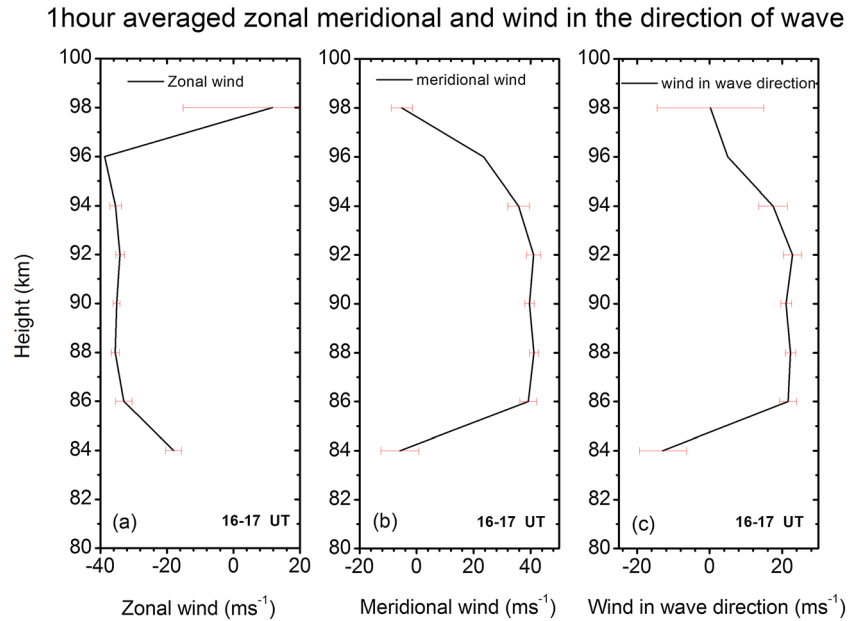


Figure 4. Variation of average winds (1 h) in the (a) zonal and (b) meridional directions during the observed wave event. (c) The winds in the direction of wave propagation are also shown. The error bars show the standard error in the observations.

horizontal as well as the upward propagation of waves, the Kolhapur (16.5°N, 74.2°E) which is difficult as wind measurements at multiple locations within the image measurements are not available. However, the wind estimates in zonal as well as meridional directions were significantly smaller than the phase velocity of wave. Overall, the data therefore suggest the propagation of waves in the north-east direction.

3.3. Mesospheric Temperatures

The thermal structure of the mesosphere is important for short-period gravity wave features. To obtain background temperature profile in upper mesospheric altitudes, we have used the MLTP and Rayleigh lidar data available on 16 March 2012; from that, we retrieved the temperature from 14:04 UT to 19:38 UT with 30 min intervals (as described by Taori *et al.* [2012]), shown in Figure 5. Together with the improved Rayleigh

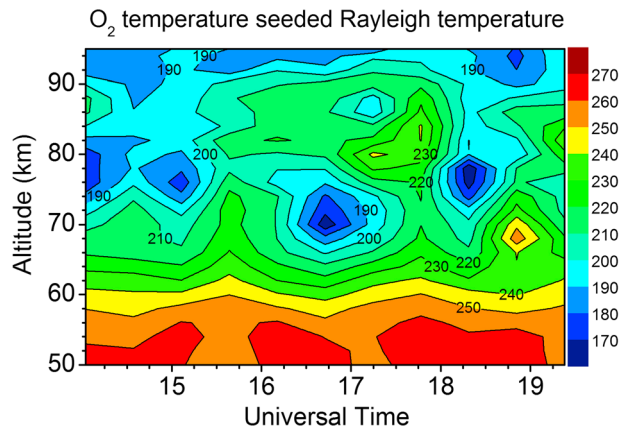


Figure 5. Contour of 30 min interval improved Rayleigh lidar temperature over Gadanki (13.5°N, 79.2°E) from 14:04 UT to 19:38 UT on 16 March 2012. The large temperature gradients in 80–95 km altitudes are noteworthy.

lidar temperature, we have used the spaceborne SABER temperature data for a wide grid encompassing 3°N to 23°N latitudes and 60°E to 100°E longitudes. On this night, the SABER passes were available during 19:30–21:30 UT with a total of 13 temperature profiles. These data were averaged to get a profile which may represent the background temperature variation nearby Gadanki (13.5°N, 79.2°E). We have plotted the nightly mean improved Rayleigh temperature estimates with mean SABER temperature in Figure 6. In this figure, the SABER temperature profiles are shown in red color lines together with their standard errors from 60 km to 105 km altitude. The improved Rayleigh tem-

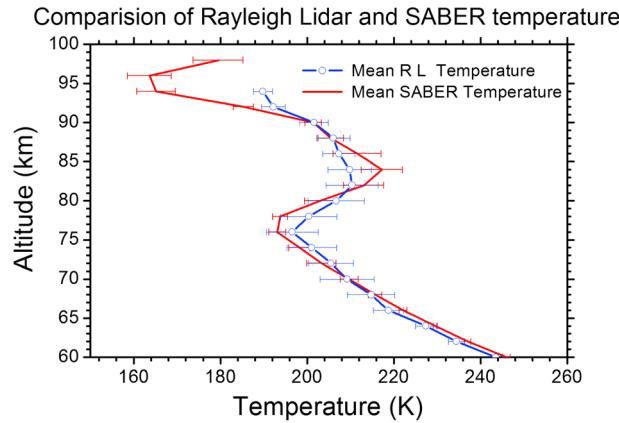


Figure 6. Comparison of the average temperature measurements for 3°N–23°N and 60°E–100°E grid on 16 March 2012 using SABER data and improved Rayleigh temperature data over Gadanki (13.5°N, 79.2°E).

perature estimates are plotted as blue lines with associated standard errors from 60 to 95 km altitudes. A good agreement between SABER data and mean Rayleigh lidar temperature estimate is evident. It is also clear that the SABER temperature shows two minima with one occurring at 76–78 km and the other occurring at 96 km altitudes. It is worth mentioning here that the lidar temperatures are shown in 60–95 km altitudes, which are somewhat lower than the peak emission altitude of O(¹S) night airglow emission. However, in general, the O(¹S) emission layer represents an altitude region of 92–102 km [e.g., *Shepherd et al.*, 1997]. Therefore, in absence of any other suitable time-resolved measurements, we have used these data to explain the observed wave event.

4. Results and Discussion

Our observations reveal the presence of a gravity wave event in O(¹S) emission, which had horizontal wavelength ~21.5 km and phase speed ~49 m s⁻¹ resulting in the periodicity ~7.3 min. This wave was traveling to the north-east direction at an azimuth angle ~65°. The meridional winds were smaller in magnitudes, which support the northward propagation, and the zonal winds were westward; therefore, these waves are not filtered out by them [*Lindzen*, 1981], which support the measurements. Quantitatively, also the estimated winds in the direction of wave propagation were sufficiently smaller than the phase velocity of wave, suggesting that wind-induced filtering did not play a significant role. This aspect of wave propagation observation over Gadanki is in agreement with earlier reports by several investigators [e.g., *Medeiros et al.*, 2003; *Mukherjee et al.*, 2010; *Li et al.*, 2011] that the waves traveling in the direction of winds are blocked if their phase speed is less than the wind amplitudes. These waves had their origin at lower altitudes as some signatures were noted in OH layer. On this night, SABER OH emission data show that occurrence of peak emission altitude is ~85 km (not shown). Around this altitude, the mean zonal wind is westward with speed of 25 ± 2 m/s, and the mean meridional wind is moving toward north with speed of 17 ± 3 m/s together with the wind in the direction of wave propagation 10 ± 2 m/s. The mean temperature around this altitude is 215 ± 5.5 K from SABER data and 208 ± 4 K from improved Rayleigh lidar data. Moreover, the change in potential temperature does not show negative value around this region (not shown). It means that there is no instability around this region. Overall, the background conditions were initially favorable for horizontal as well as vertical propagation of waves in north-east direction.

Interesting part of the present investigation is that the observed waves at O(¹S) emission altitudes clearly show the transformation from 21.5 km scales to very small scales (<8 km) and ultimately absorption of waves in the background in about 20 min duration. To identify whether wave could propagate further upward and the cause of this dissipation, we carry out the following investigations.

1. Calculate the frequency (and period) of the natural oscillations (N²) values using the following equation:

$$N^2 = \frac{g}{T} \left(\frac{dT}{dz} + \frac{g}{c_p} \right), \tag{1}$$

where *N* is the Brunt-Väisälä frequency (rad s⁻¹), *g* is the acceleration due to gravity at mesospheric altitude (9.5 m s⁻²), *c_p* is the specific heat capacity (1004 J kg⁻¹ K⁻¹), *T* is the background temperature (K), and $\frac{dT}{dz}$ is the change in the temperature with respect to altitude.

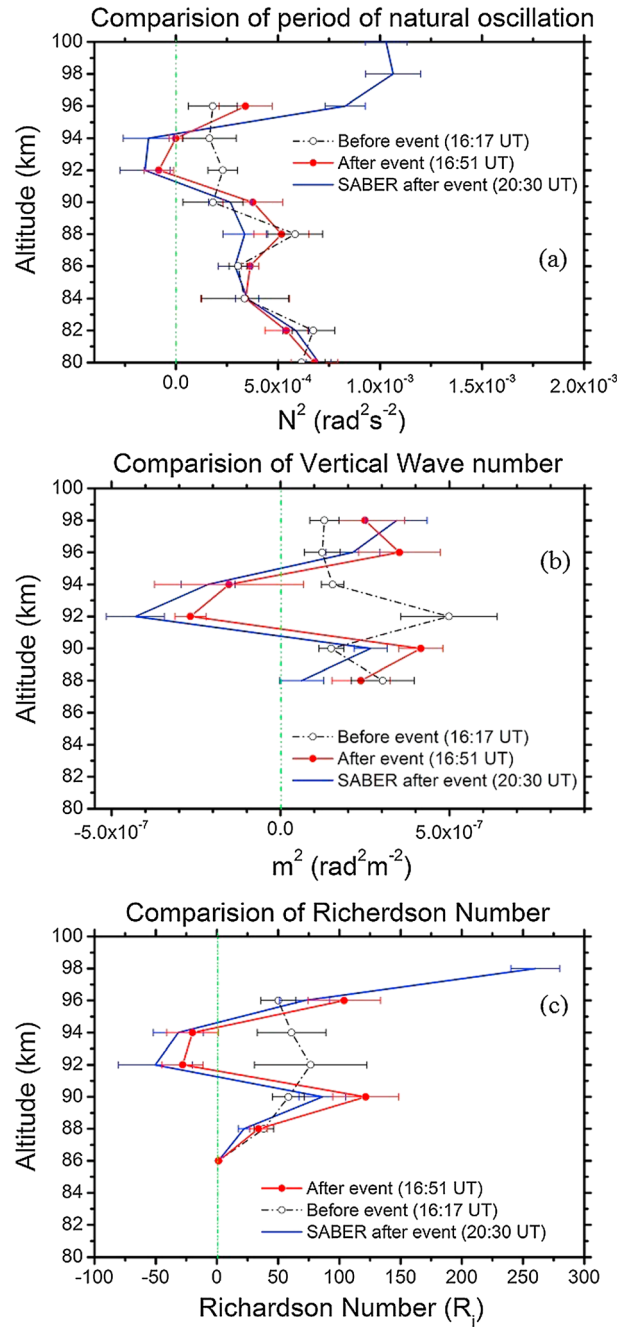


Figure 7. (a) The variation of square of the Brunt-Väisälä frequency (N^2) and its standard errors for before (black color dash-dotted line) and after the event (red color for Rayleigh data and blue color for SABER data), (b) the square of the vertical wave number (m^2) and its standard errors for before (black color dash-dotted line) and after the event (red color for Rayleigh data and blue color for SABER data), and (c) the Richardson number and their standard errors for before (black color dash-dotted line) and after the event (red color for Rayleigh data and blue color for SABER data) with respect to the altitude.

and after the events are shown in Figure 7b, while the Richardson number (R_i) and their error estimates before and after the events are shown in Figure 7c. It is important to note that although the upward propagation of these waves was possible from 85 km to 90 km, there was a strong

2. Calculate the m^2 values so that we may know whether wave could propagate further using the following equation [e.g., Nappo, 2002]:

$$m^2 = \frac{N^2}{(c - U)^2} + \frac{U''}{(c - U)} - \frac{1}{H_s} \frac{U'}{(c - U)} - k^2, \quad (2)$$

where m is the vertical wave number (rad m^{-1}), N is the Brunt-Väisälä frequency (rad s^{-1}), c is the observed phase speed of wave (m s^{-1}), U is the wind in the direction of wave propagation (m s^{-1}), U' is the first derivative (dU/dz) of wind in the wave direction, U'' shows the second derivative (d^2U/dz^2) of wind in wave direction, k is the horizontal wave number, and H_s is representing the atmospheric scale height ($H_s = \frac{R_d T}{g}$, where T is the background temperature and R_d is the gas constant for dry air ($287 \text{ J kg}^{-1} \text{ K}^{-1}$).

3. Calculate the Richardson number to identify the instability process behind the observed wave dissipation event using the equation as follows [e.g., Nappo, 2002]:

$$Ri = \frac{N^2}{(u'^2 + v'^2)}, \quad (3)$$

where Ri is the Richardson number, u' is the first derivative of mean zonal wind, and v' is the first derivative of mean meridional wind.

We have calculated the square of the Brunt-Väisälä frequency, vertical wave number, and Richardson number before (16:17 UT) and after (16:51 UT) the wave event by using the MF wind data, improved Rayleigh lidar temperature as well as SABER temperature data (after the event at around 20:30 UT). Results of these exercises are shown in Figure 7. The N^2 values and their standard errors before (black color dash-dotted line) and after the event (red color line for Rayleigh data and blue color line for SABER data) are shown in Figure 7a. Similarly, the m^2 values and their standard errors before

altitude region at 92–93 km, which did not allow them to propagate further. Therefore, it is possible that we were observing a trapped wave in this region. There is another possibility that as this wave was allowed to propagate from 85 to 90 km altitude and wind-induced reduction in vertical wavelength may induce self-absorption within the airglow layer, resulting in the decreased amplitude to the extent that they become invisible. In this regard, with the help of period of natural oscillation (~6.5 min), horizontal wavelength (~21.5 km), and the observed wave period (~7.3 min), the calculated vertical wavelength [Hines, 1960] is estimated to be ~19 km (as simplified relation suggests that vertical wavelength/horizontal wavelength = period of natural oscillation/wave period), while the typical layer thickness is ~8 km; therefore, we rule out such self-absorption of wave. Another possibility is that multiple-wave processes may be having destructive interference, which exhibited into faded features as noted. In order to estimate this effect, we have removed the background and large-scale structure by subtracting the individual images from the average of 20 images (nearly 1 and 0.5 h average). Although we cannot negate this processes, there is no supporting evidence for the same. More appealing aspect is that square of the Brunt-Väisälä frequency values at 91–93 km altitudes show negative values. Together with this, the square of the vertical wave number(m^{-2}) values also show negative values at around 91–93 km altitudes. These values suggest that most possibly, these waves would be absorbed by the ambient, which supports the occurrence of instability process. To identify this, we looked at the Richardson number (Ri); it is the index of atmospheric stability. We note that the Ri becomes negative at around 92–95 km altitudes. It is important to state here that convective instability occurs when Ri values are less than 0 (or N^2 is negative) and when Ri values are between 0 and 0.25, dynamic instability occurs [e.g., Yamada et al., 2001; Hecht, 2004; Suzuki et al., 2011]. Therefore, our results show that in present case, the wave dissipation occurred due to convective instability. Of importance is that Yamada et al. [2001] clearly showed the evidences that the wave observed in their data broke into turbulence due to dynamical instability, while our results show that the observed wave dissipation occurred due to convective instability.

In summary, our data show the evidence of a gravity wave which was absorbed into background within 15 min. We examined the propagation conditions of the observed wave and the cause of dissipation. Our further step will be to understand such cases and their causative mechanisms based on a substantially larger data set. This is important in understanding the climatology of short-period gravity waves from Indian sector and their impacts on the global circulation in the middle and upper atmosphere, which are least understood.

Acknowledgments

The airglow experiments carried out at NARL are supported by Department of Space, Government of India. Authors thank Liyakath Basha, V. Kamalakar, G. Ravikumar, and Rounaq Goenka for their help in the routine operation of airglow instruments and fruitful discussions. The observations made can be available by sending a request to the corresponding author (alok.taori@gmail.com), or by filling data request form at www.ldc.narl.gov.in.

Alan Rodger thanks the reviewers for their assistance in evaluating this paper.

References

- Alexander, M. J., et al. (2010), Recent developments in gravity-wave effects in climate models and the global distribution of gravity-wave momentum flux from observations and models, *Q. J. R. Meteorol. Soc.*, *136*, 1103–1124, doi:10.1002/qj.637.
- Cai, X., T. Yuan, Y. Zhao, P.-D. Pautet, M. J. Taylor, and W. R. Pendleton Jr. (2014), A coordinated investigation of the gravity wave breaking and the associated dynamical instability by a Na lidar and an Advanced Mesosphere Temperature Mapper over Logan, UT (41.7°N, 111.8°W), *J. Geophys. Res. Space Physics*, *119*, 6852–6864, doi:10.1002/2014JA020131.
- Fritts, D. C. (1989), A review of gravity wave saturation processes, effects, and variability in the middle atmosphere, *Pure Appl. Geophys.*, *130*(2/3), 343–371.
- Fritts, D. C., and Alexander M. J. (2003), Gravity wave dynamics and effects in the middle atmosphere, *Rev. Geophys.*, *41*(1), 1003, doi:10.1029/2001RG000106.
- Ghodpage, R. N., A. Taori, P. T. Patil, S. Gurubaran, A. K. Sharma, S. Nikte, and D. Nade (2014), Airglow measurements of gravity wave propagation and damping over Kolhapur (16.5°N, 74.2°E), *Int. J. Geophys.*, doi:10.1155/2014/514937.
- Hauchecorne, A., and M.-L. Chanin (1980), Density and temperature profiles obtained by lidar between 30 and 70 km, *Geophys. Res. Lett.*, *7*, 565–568, doi:10.1029/GL007i008p00565.
- Hecht, J. H. (2004), Instability layers and airglow imaging, *Rev. Geophys.*, *42*, RG1001, doi:10.1029/2003RG000131.
- Hines, C. O. (1960), Internal atmospheric gravity waves at ionospheric heights, *Can. J. Phys.*, *38*, 1441–1481.
- Kamalakar, V., A. Taori, K. Raghunath, S. V. B. Rao, and A. Jayaraman (2013), On Rayleigh lidar capability enhancement for the measurement of short-period waves at upper mesospheric altitudes, *Int. J. Remote Sens.*, *34*(21), 7474–7486, doi:10.1080/01431161.2013.822599.
- Lakshmi Narayanan, V., S. Gurubaran, and K. Emperumal (2010), Airglow imaging observations of small-scale structures driven by convective instability in the upper mesosphere over Tirunelveli (8.7°N), *J. Geophys. Res.*, *115*, D19119, doi:10.1029/2009JD012937.
- Li, Z., A. Z. Liu, X. Lu, G. R. Swenson, and S. J. Franke (2011), Gravity wave characteristics from OH airglow imager over Maui, *J. Geophys. Res.*, *116*, D22115, doi:10.1029/2011JD015870.
- Lindzen, R. S. (1981), Turbulence and stress owing to gravity wave and tidal breakdown, *J. Geophys. Res.*, *86*, 9707–9714, doi:10.1029/JC086iC10p09707.
- Mayr, H. G., J. G. Mengel, C. A. Reddy, K. L. Chan, and H. S. Porter (2000), Properties of QBO and SAO generated by gravity waves, *J. Atmos. Sol. Terr. Phys.*, *62*, 1135–1154.
- Medeiros, A. F., M. J. Taylor, H. Takahashi, P. P. Batista, and D. Gobbi (2003), An investigation of gravity wave activity in the low-latitude upper mesosphere: Propagation direction and wind filtering, *J. Geophys. Res.*, *108*(D14), 4411, doi:10.1029/2002JD002593.
- Meriwether, J. W. (1984), Ground based measurements of mesospheric temperatures by optical means, in *International Council of Scientific Unions Middle Atmosphere Program Handbook MAP*, vol. 13, edited by R. Vincent, pp. 1–18, NASA, Green belt, Md.

- Mukherjee, G. K., R. Pragati Shikha, N. Parihar, R. Ghodpage, and P. T. Patil (2010), Studies of the wind filtering effect of gravity waves observed at Allahabad (25.45°N, 81.85°E) in India, *Earth Planet Space*, *62*, 309–318, doi:10.5047/eps.2009.11.008.
- Nappo, C. J. (2002), *An Introduction to Atmospheric Gravity Waves*, *Int. Geophys. 293 Ser.*, vol. 85, Academic Press, San Diego, Calif.
- Pautet, P.-D., M. J. Taylor, A. Z. Liu, and G. R. Swenson (2005), Climatology of short-period gravity waves observed over northern Australia during the Darwin Area Wave Experiment (DAWEX) and their dominant source regions, *J. Geophys. Res.*, *110*, D03S90, doi:10.1029/2004JD004954.
- Rajaram, R., and S. Gurubaran (1998), Seasonal variabilities of low-latitude mesospheric winds, *Ann. Geophys.*, *16*, 197–204.
- Remsberg, E. E., et al. (2008), Assessment of the quality of the version 1.07 temperature-versus-pressure profiles of the middle atmosphere from TIMED/SABER, *J. Geophys. Res.*, *113*, D17101, doi:10.1029/2008JD010013.
- Shepherd, G. G., N. J. Siddiqi, R. H. Wines, and S. Zhang (1997), Airglow measurements of possible changes in the ionosphere and middle atmosphere, *Adv. Space Res.*, *20*(11), 2127–2135.
- Siva Kumar, V., P. B. Rao, and M. Krishnaiah (2003), Lidar measurements of stratosphere-mesosphere thermal structure at a low latitude: Comparison with satellite data and models, *J. Geophys. Res.*, *108*(D11), 4342, doi:10.1029/2002JD003029.
- Smith, A. K. (2012), Global dynamics of MLT, *Surv. Geophys.*, *33*, 1177–1230, doi:10.1007/s10712-012-9196-9.
- Smith, S. M., J. Scheer, E. R. Reisin, J. Baumgardner, and M. Mendillo (2006), Characterization of exceptionally strong mesospheric wave events using all-sky and zenith airglow observations, *J. Geophys. Res.*, *111*, A09309, doi:10.1029/2005JA011197.
- Suzuki, S., K. Shiokawa, A. Z. Liu, Y. Otsuka, T. Ogawa, and T. Nakamura (2009), Characteristics of equatorial gravity waves derived from mesospheric airglow imaging observations, *Ann. Geophys.*, *27*, 1625–1629.
- Suzuki, S., M. Tsutsumi, S. E. Palo, Y. Ebihara, M. Taguchi, and M. Ejiri (2011), Short-period gravity waves and ripples in the South Pole mesosphere, *J. Geophys. Res.*, *116*, D19109, doi:10.1029/2011JD015882.
- Taori, A., M. Taylor, and J. France (2005), Terdiurnal wave signatures in the upper mesospheric temperature and their association with the wind field at low latitudes (20°N), *J. Geophys. Res.*, *110*, D09S06, doi:10.1029/2004JD004564.
- Taori, A., V. Kamalakar, and A. Jayaraman (2011), First measurement of upper mesospheric semiannual oscillations using ground based airglow measurements from Indian low latitudes, *Adv. Space Res.*, *49*, 937–942, doi:10.1016/j.asr.2011.12.016.
- Taori, A., A. Jayaraman, K. Raghunath, and V. Kamalakar (2012), A new method to derive middle atmospheric temperature profiles using a combination of Rayleigh lidar and O₂ airglow temperatures measurements, *Ann. Geophys.*, *30*, 27–32, doi:10.5194/angeo-2012.
- Taori, A., A. Jayaraman, and V. Kamalakar (2013), Imaging of mesosphere-thermosphere airglow over Gadanki (13.50°N, 79.20°E): First results, *J. Atmos. Sol. Terr. Phys.*, *93*, 21–28, doi:10.1016/j.jastp.2012.11.007.
- Taylor, M. (1997), A review of advances in imaging techniques for measuring short period gravity waves in the mesosphere and lower thermosphere, *Adv. Space Res.*, *19*, 667–676.
- Yamada, Y., H. Fukunishi, T. Nakamura, and T. Tsuda (2001), Breaking of small-scale gravity wave and transition to turbulence observed in OH airglow, *Geophys. Res. Lett.*, *28*, 2153–2156, doi:10.1029/2000GL011945.